LAWRENCE
LIVERMORE
NATIONAL
LABORATORY

UCRL-CONF-209424

A Computational Model with Experimental Validation for DNA Flow in Microchannels

A. Nonaka, S. Gulati, D. Trebotich, G. H. Miller, S. J. Muller, D. Liepmann

February 4, 2005

Nanotech 2005
Anaheim, CA, United States
May 8, 2005 through May 12, 2005

A Computational Model with Experimental Validation for DNA Flow in Microchannels

A. Nonaka*‡, S. Gulati††, D. Trebotich‡, G. H. Miller*, S. J. Muller†† and D. Liepmann††

*University of California, Davis, Department of Applied Science
One Shields Ave., Davis, CA, USA, 95616-8254, ajnonaka@ucdavis.edu
‡ Lawrence Livermore National Laboratory, Livermore, CA, USA
†† University of California, Berkeley, CA, USA

ABSTRACT

We compare a computational model to experimental data for DNA-laden flow in microchannels. The purpose of this work in progress is to validate a new numerical algorithm for viscoelastic flow using the Oldroyd-B model. Our numerical approach is a stable and convergent polymeric stress-splitting scheme for viscoelasticity. We treat the hyperbolic part of the equations of motion with an embedded boundary method for solving hyperbolic conservation laws in irregular domains. We enforce incompressibility and evolve velocity and pressure with a projection method. Our experiments are performed using epifluorescent microscopy and digital particle image velocimetry to measure velocity fields and track the conformation of biological macromolecules. We present results comparing velocity fields and the observations of computed fluid stress on molecular conformation in various microchannels.

Keywords: viscoelasticity, Oldroyd-B, hyperbolic conservation laws, embedded boundaries, digital particle image velocimetry

1 INTRODUCTION

We consider flow of an incompressible viscoelastic fluid at the microscale. Viscoelasticity is an appropriate model for particle-laden biological fluids consisting of macromolecules including DNA. We begin by summarizing our equations of motion, algorithm and experimental techniques followed by a comparison of computational and experimental data. Included are data for several contraction geometries found in bioMEMS devices, with a direct comparison of velocity profiles and possible effects of computed fluid stress on observed molecular deformation in [5].

2 EQUATIONS OF MOTION

The equations of motion are the incompressible Navier-Stokes equations coupled to the Oldroyd-B polymeric stress equation:

$$\rho\left(\frac{\partial \mathbf{u}}{\partial t} + (\mathbf{u}\cdot\nabla)\mathbf{u}\right) = -\nabla p + \mu_s \Delta \mathbf{u} + \nabla\cdot\boldsymbol{\tau}, \quad (1)$$

$$\nabla\cdot\mathbf{u} = 0, \quad (2)$$

$$\frac{\partial \boldsymbol{\tau}}{\partial t} + (\mathbf{u}\cdot\nabla)\boldsymbol{\tau} - \nabla\mathbf{u}\cdot\boldsymbol{\tau} - \boldsymbol{\tau}\cdot(\nabla\mathbf{u})^T = \frac{1}{\lambda}\left[\mu_p(\nabla\mathbf{u} + (\nabla\mathbf{u})^T) - \boldsymbol{\tau}\right]. \quad (3)$$

Here, ρ is the fluid density, $\mathbf{u}$ is the velocity, p is the isotropic pressure, $\boldsymbol{\tau}$ is the fluid stress, λ is the relaxation time and μ_s and μ_p are the solvent and polymeric contributions to the total viscosity.

3 ALGORITHM

We approach the problem numerically with a polymeric stress splitting scheme which is stable and convergent for the full range of viscoelastic flows [1]. Here the equations of motion have been made suitable for the approach in [3] for solving hyperbolic conservations laws on irregular domains. In order to enforce the incompressibility restraint, we use the higher-order projection method described in [2].

We begin by intersecting our domain with a cell-centered Cartesian grid. In order to obtain a high order approximation for our fluxes, we first cast the equations in linear advection form:

$$\frac{\partial W}{\partial t} + \sum_{i=0}^{D-1} A_i(W)\frac{\partial W}{\partial x_i} = S_W, \quad (4)$$

where W is the vector of primitive variables, D is the dimensionality of the problem, A_i are matrices and S_W is the primitive source term vector. We then employ Taylor series and characteristic tracing to obtain face-centered, time-centered values for the primitive variables. To update the cells, we use the conservation form:

$$\frac{\partial U}{\partial t} + \nabla\cdot F(U) = S_U, \quad (5)$$

where U is the vector of conserved variables, F is the vector of fluxes and S_U is the conservative source term vector. We project the velocity field in order to enforce the incompressibility constraint.

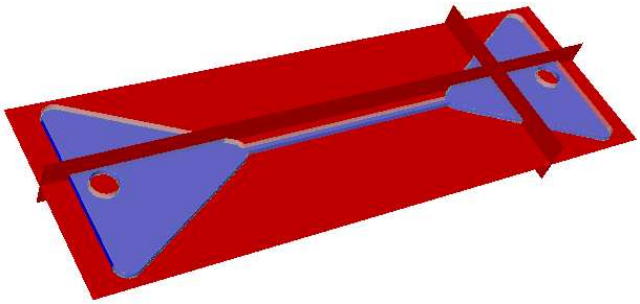

Figure 1: Embedded boundary representation of contraction/expansion device. Fluid enters/exits device through tubes attached to triangular reservoirs at indicated locations.

To handle irregular geometries, we use the embedded boundary method, which is a volume of fluid method that takes a "cookie cutter" approach to irregular domain boundaries on Cartesian grids. Cut cells exist near boundaries and are treated with advanced discretization stencils [3], [4].

4 EXPERIMENTS

To obtain velocity fields in components of bioMEMS devices, we use the digital particle image velocimetry (DPIV) technique described by Devasenathipathy et al. [6]. DPIV combines epifluorescent microscopy, where fluorescent seed particles are imaged at successive timesteps, and image interrogation algorithms to calculate the velocity fields. We measure the orientation and deformation of λ-DNA molecules using the technique described in [5]. This experimental technique involves marking the λ-DNA molecules with a fluorescent dye and imaging the molecules with epifluorescent microscopy. Statistical data is obtained by tracking molecules that pass through particular regions in the microchannel rather than tracking individual particles.

We measure the viscosities μ_p and μ_s, and use the

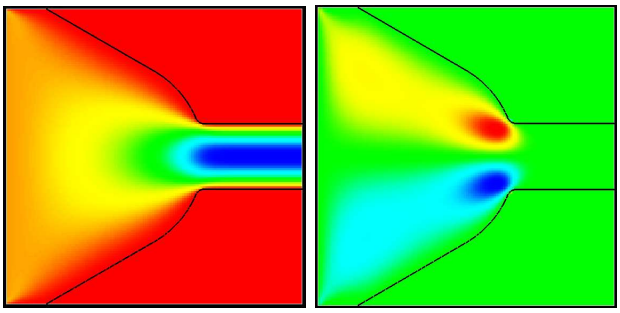

Figure 2: Computed results for x-velocity field; 0 μm/s (red) to 175μm/s (blue) and y-velocity field; -33μm/s (red) to 33μm/s (blue) for the rounded contraction device.

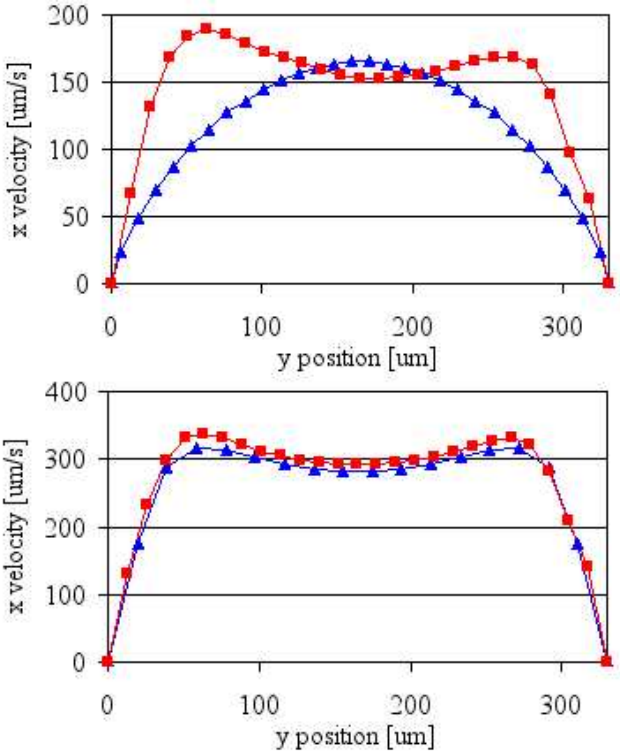

Figure 3: Experimental (red with squared) vs. computational (blue with triangles) x-velocity profile comparison at point "B" using 2D viscoelastic model and 3D viscous model.

Rouse model to obtain the relaxation time:

$$\lambda = \frac{[\mu]\mu_s M}{RT}, \tag{6}$$

where M is the molecular weight of λ-DNA, R is the gas constant and T is temperature. The intrinsic viscosity, $[\mu]$, is calculated using:

$$\mu_p + \mu_s \approx \mu_s(1 + [\mu]c), \tag{7}$$

where c is the concentration of λ-DNA in solution. Device fabrication, imaging instrumentation and fluid characterization are described in detail in [5].

5 RESULTS

We use the convention that the direction of positive flow is the $+x$ direction while the width and depth are the y and z direction, respectively. All velocity fields are measured at the median depth of the channel. Unless otherwise specified, all computations are performed using a 2D viscoelastic model.

5.1 Rounded Contraction Velocity Profiles

Our first geometry is the rounded contraction geometry used in [5]. Two triangular reservoirs are connected by a narrow rectangular channel with length L = 8mm. The depth of the entire device is d = 60μm and the width of the narrow channel is w = 330μm. See Figure 1 for an embedded boundary representation of this geometry. We compute velocity fields in the region before and after the contraction. The experimentally obtained parameters are: Q = 10μL/hr, ρ = 1g/mL, μ_s = 25.0cP, μ_p = 0.975cP and λ = 0.416s.

The computed x and y velocity fields are shown in Figure 2. In Figure 3 we compare x-velocity profiles for computational and experimental data at the contraction cross section. We note that our experiment yields a "top-hat" x-velocity profile at the contraction, yet our 2D computations do not. Using the same contraction geometry, we have previously performed computations for viscous flow in both 2D and 3D. We only see evidence of a top-hat velocity profile with a 3D model, as shown in Figure 3. We believe the large channel width-to-depth ratio is the cause of this phenomena, and therefore a 2D model cannot capture this 3D effect. An extension of our viscoelastic model to 3D is being developed which will investigate this phenomena.

5.2 Rounded Contraction Stress Profiles

We now wish to examine the effect of fluid stress on the stretching of λ-DNA molecules. We present normal stress (τ_{xx}) and shear stress (τ_{yx}) profiles in Figure 4. Note that due to conservation of angular momentum, the stress tensor is symmetric, and therefore $\tau_{xy} = \tau_{yx}$. We will compare our stress profiles with experimental data on λ-DNA molecule conformation.

The effect of normal stress stretching is represented by τ_{xx}. In this geometry, we predict normal stress down

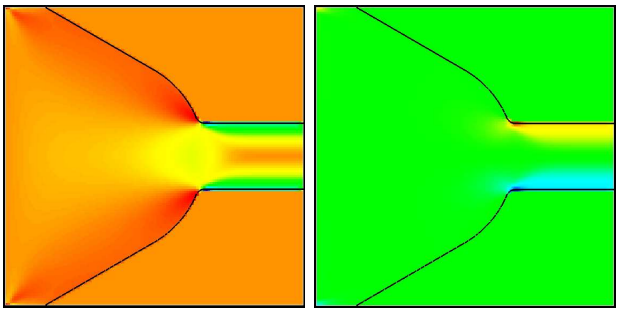

Figure 4: Computed results for normal stress field; -10mg/(cm-s^2) (red) to 61mg/(cm-s^2) (blue) and shear stress field; -48mg/(cm-s^2) (red) to 48mg/(cm-s^2) (blue) for the rounded contraction device.

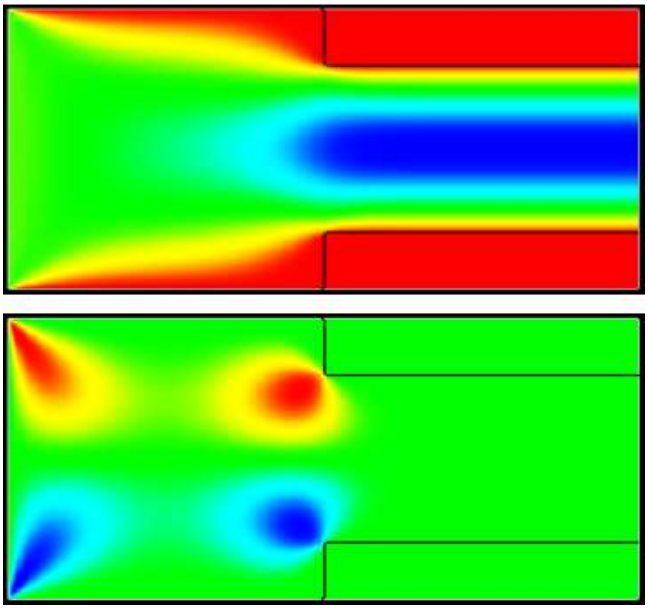

Figure 5: Computed results for x-velocity field; 0μm/s (red) to 275μm/s (blue) and y-velocity field; -45μm/s (red) to 45μm/s (blue) for the abrupt contraction geometry.

the centerline as the fluid accelerates inside the contraction and near the walls in the contracted channel. There is no normal stress component down the centerline in the contracted channel. The images in [5] support this centerline normal stress profile, as the particles stretch from their original position to the increased lengths at the contraction, and then relax back to their original configuration as they pass downstream.

It has been observed in [5] that, within the contraction, the particles near walls appear more stretched out than the particles near the centerline. Our computations indicate that the magnitude of both shear and normal stress is higher near wall locations than near the centerline. Further investigation is required to determine the relative influence of each type of stress near the wall locations on molecular stretching.

5.3 Abrupt Contraction Velocity Profiles

Our second geometry is an abrupt contraction geometry. The depth of the device is d = 100μm, the pre-contraction width is W = 100μm and the post-contraction width is w = 60μm. The experimentally obtained parameters are: Q = 10μL/hr, ρ = 1g/mL, μ_s = 25.0cP, μ_p = 0.975cP and λ = 0.416s.

The computed x and y velocity fields are shown in Figure 5. We compare x-velocity profiles for computational and experimental data at cross sections located at 150μm before and 150μm after the contraction. Our

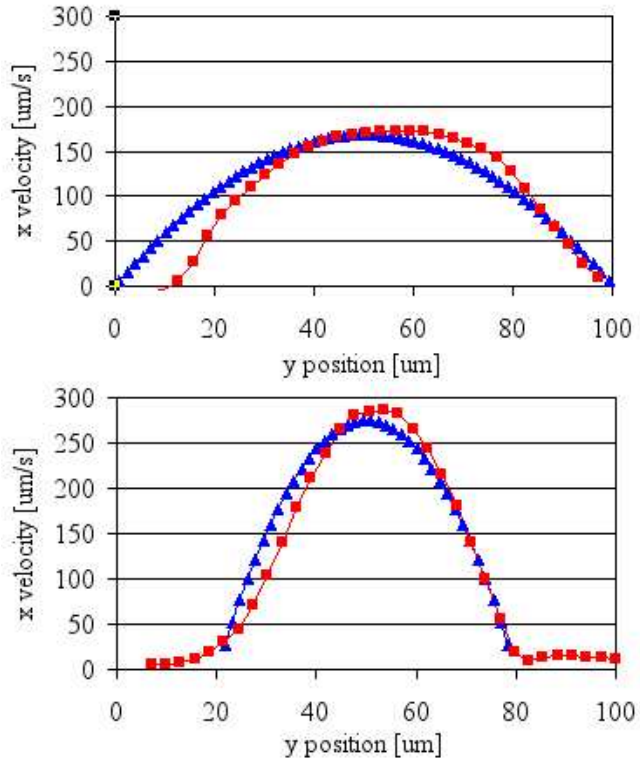

Figure 6: Experimental (red with squares) vs. computational (blue with triangles) x-velocity comparison at 150μm prior to and 150μm post contraction.

model compares well with the experimental results for both locations.

6 CONCLUSION

We provide comparison between computation and experiment for non-Newtonian, viscoelastic flow in irregular microdevice geometries. The velocity fields compare well, but a 3D model is required to capture certain experimentally observed effects, especially where large width to depth ratios exist. The stress fields are consistent with experimental observations for macromolecular conformation. This work provides the foundation for computing fluid flows in more complicated microdevice components as well as biological systems. Future work involves the inclusion of a particle representation to our continuum model, as well as an extension to adaptive mesh refinement (AMR), where we locally increase the spatial resolution in regions of high gradients.

ACKNOWLEDGMENT

This work was performed under the auspices of the U.S. Department of Energy by the University of California, Lawrence Livermore National Laboratory under contract No. W-7405-Eng-48. Work at UC Davis was partially supported by the US DOE MICS Division under contract number DE-FG02-03ER25579.

REFERENCES

[1] D. Trebotich, P. Colella and G. H. Miller, J. Comp. Phys., to appear, 2005.

[2] J. B. Bell, P. Colella and H. M. Glaz, J. Comp. Phys., 85, 257-283, 1989.

[3] P. Colella, D. T. Graves, B. J. Keen and D. Modiano, submitted, 2004.

[4] P. Schwartz, M. Barad, P. Colella, T. Ligocki, submitted, 2004.

[5] P. Shrewsbury, S. J. Muller and D. Liepmann, Biomedical Microdevices, 3, 225-238, 2001.

[6] S. Devasenathipathy, J. Santiago, S. Werely, C. Meinhart and K. Takehara, Experiments in Fluids, 34, 502-514, 2003.